arXiv:1608.02376v1 [cond-mat.str-el] 8 Aug 2016

Positron spectroscopy of point defects in the skyrmion-lattice compound MnSi

Markus Reiner[1,2], Andreas Bauer[1], Michael Leitner[2], Thomas Gigl[1,2], Wolfgang Anwand[3],Maik Butterling[3], Andreas Wagner[3], Petra Kudejova[2], Christian Pfleiderer[1], and Christoph Hugenschmidt[1,2*]

[1]Physik-Department, Technische Universität München, 85748 Garching, Germany
[2]Heinz Maier-Leibnitz Zentrum (MLZ), Technische Universität München, 85748 Garching, Germany
[3]Institut für Strahlenphysik, Helmholtz-Zentrum Dresden-Rossendorf, 01314 Dresden, Germany

Abstract

Outstanding crystalline perfection is a key requirement for the formation of new forms of electronic order in a vast number of widely different materials. Whereas excellent sample quality represents a standard claim in the literature, there are, quite generally, no reliable microscopic probes to establish the nature and concentration of lattice defects such as voids, dislocations and different species of point defects on the level relevant to the length and energy scales inherent to these new forms of order. Here we report an experimental study of the archetypical skyrmion-lattice compound MnSi, where we relate the characteristic types of point defects and their concentration to the magnetic properties by combining different types of positron spectroscopy with ab-initio calculations and bulk measurements. We find that Mn antisite disorder broadens the magnetic phase transitions and lowers their critical temperatures, whereas the skyrmion lattice phase forms for all samples studied underlining the robustness of this topologically non-trivial state. Taken together, this demonstrates the unprecedented sensitivity of positron spectroscopy in studies of new forms of electronic order.

Introduction

Intermetallic compounds attract tremendous interest as a playground for novel electronic phases, such as unconventional superconductivity, partial forms of the electronic and spin order, emergent behaviour such as magnetic monopoles in the spin ices and frustration in spin liquids. In general, the preparation of high-quality single crystals of the materials of interest is extremely demanding, since a large number of mechanisms lead to the formation of intrinsic point defects. Examples include the formation due to configuration entropy, kinetically inhibited atomic motion during solidification and frozen-in disorder. The different species of defects comprise of, e.g., point defects such as vacancies and antisite disorder,

*E-mail: christoph.hugenschmidt@frm2.tum.de

dislocations or vacancy clusters. Despite their great relevance, the qualitative and quantitative identification of point defects has been very challenging technically. For instance, scanning tunneling microscopy is a surface sensitive probe only, whereas transmission electron microscopy introduces ambiguities, as the sample has to be machined thinned and prepared mechanically. Further, the degree of long-range order is conventionally accessible by diffraction techniques. Yet, point defect concentrations cannot be resolved below 10^{-2}.

In this paper, we demonstrate how to obtain microscopic insights on the existence, nature and quantity of defects in intermetallic compounds. We combine various positron-based techniques and ab-initio calculations of point defect thermodynamics for the identification of the defect species and the quantitative determination of the defect density. This allows us to elucidate their influence on the magnetic and transport properties in the itinerant-electron magnet MnSi.

For our study we have selected MnSi as an important show-case of several aspects of new forms of electronic order. Notably, MnSi and related compounds in recent years have attracted great interest due to the formation of a regular arrangement of spin whirls forming a so-called skyrmion lattice at finite magnetic fields in a small phase pocket just below T_c [1–10]. The non-trivial topological winding of these whirls gives rise to an emergent electrodynamics, in which each skyrmion carries one quantum of emergent magnetic flux [11–13]. The emergent electrodynamics is at the heart of exceptionally strong spin transfer torques overcoming defect related pinning. This has generated great interest to exploit skyrmions in spintronics devices. Another important facet of the magnetic properties of MnSi is the paramagnetic to helimagnetic transition, which represents the first unambiguous example of a fluctuation-induced first order transition as long predicted by Brazovskii in the context of soft matter. As for the skyrmion lattice phase the effects of tiny defect concentrations appear to be of central importance. Last but not least, high pressure studies in MnSi have revealed an extended non-Fermi liquid regime, where both the exponent and prefactor of the resistivity are essentially independent of the residual resistivity [15–17]. These various aspects of the importance of defects are underscored by the metallurgical properties of MnSi, which appear to be particularly amenable to the preparation of large, virtually perfect single crystals. In turn, MnSi represents a show-case par excellence in which the influence of low defect concentrations on novel electronic properties may be studied.

MnSi belongs to the cubic B20 compounds with the space group $P2_13$ lacking inversion symmetry. MnSi melts congruently at 1270 °C and large single crystals may be readily grown from the melt using methods such as Czochralsky, Bridgman, and inductively or optically heated float-zoning [14]. The resulting samples readily show residual resistivity ratios (RRR) between 50 and 100, where carefully annealed specimens reach values as high as 1000 [15]. At ambient pressure, however, small deviations of the transition temperatures and the shapes of the corresponding thermodynamic signatures were reported for samples with different RRR [18–20]. The latter also seems to influence the possibility to metastably extend the skyrmion lattice pocket at large hydrostatic pressures under field-cooling [21]. However, neither the density nor the type of

lattice defects in single-crystal MnSi has been addressed before. Knowledge of the defect structure in turn is key to understanding phenomena such as the very weak energy scales controlling the Brazovskii transition, the depinning of the skyrmion lattice under electrical currents [22–24], the dynamics of the topological unwinding of skyrmions [25], or the emergence of non-Fermi liquid behavior at high pressures [26].

Given the importance of any of these topics, we decided to study the point defects in MnSi in a series of optically float-zoned single crystals by means of positron annihilation spectroscopy. In combination with calculations of the effective formation energies of point defects this allows us to determine the species and density of defects quantitatively. Measurements of the specific heat and the ac susceptibility demonstrate that the RRR is not sufficient to characterize a sample of MnSi, as specimens with the same RRR but different dominant defect species show discrepancies in the thermodynamic signatures of the magnetic phase transitions.

Results and Discussion

For our study ten single crystals of MnSi were grown by means of optical floating-zoning [27,28]. We investigated the influence of two growth parameters, namely the growth rate, v, and the composition of the feed rods represented by the Mn excess, x, of the initial net weight of $Mn_{1+x}Si$, $-0.01 \leq x \leq 0.04$. We induced this Mn excess in order to compensate evaporative losses of Mn caused by its high vapor pressure during crystal preparation. The cylinders of the single crystals (see Fig. 1(a)) were investigated by positron annihilation lifetime spectroscopy (PALS) and the end discs by coincident Doppler broadening spectroscopy (CDBS). Prompt gamma activation analysis (PGAA) [29] results were consistent with a stoichiometric composition within the estimated error of 1.5 at.%. For all specimens we expect the same total density of impurity atoms originating from the starting elements below $5 \cdot 10^{-5}$.

The RRR of all samples studied is shown in Fig. 1(b). Additionally, the values for all crystals are given in Tab. 1 together with the other important measured parameters introduced later. The start (blue) and end (red) of the single crystals exhibit qualitatively similar behavior, where both low and high values of x lead to low RRRs around 40. A maximum in the RRR, expected for a minimal total defect concentration, is obtained for a slight initial Mn excess as consistent with a compensation of the observed evaporation of Mn during crystal growth. The small systematic variations between the start and the end of the crystals may be attributed to the different temperature history during growth where the start stayed at elevated temperatures for a longer period of time leading to larger losses of Mn. In the parameter range studied, the growth rate had no significant influence on the RRR.

The detected normalized CDB spectra are shown in Fig. 2(a) after division by the spectrum for $x = -0.01$ as so-called ratio curves, R_x. The spectra are described very well by linear combinations of $R_{-0.01}$ and $R_{0.04}$ as depicted by solid

lines. Here, the fitted weighting factor f_x is defined by $f_{-0.01} = 0$ and $f_{0.04} = 1$. The measured ratio curves R_x were compared to calculated ones, namely $R_{\text{b-VMn}}$ and $R_{\text{b-VSi}}$ of defect free bulk MnSi using either the spectra characteristic for annihilation in Mn vacancies V_{Mn} or Si vacancies V_{Si} as reference. As shown in Fig. 2(a), $R_{\text{b-VMn}}$ describes well $R_{0.04}$ for large momenta, $p_{\text{L}} > 15 \cdot 10^{-3}\, m_0 c$, where the calculation method works with high reliability [30–33]. Hence, for $x = 0.04$ most positrons annihilate in the bulk. For $x \leq 0$ the spectra hardly differ, suggesting that essentially all positrons annihilate in V_{Mn} (saturation trapping).

In order to determine the fraction, η_{b}, of positrons annihilating in the defect-free bulk for $x = 0.04$, we compared the areas enveloped by $R_{\text{b-VMn}} - 1$ and $R_{0.04} - 1$ in the range $15.9 \cdot 10^{-3}\, m_0 c < p_{\text{L}} < 39.5 \cdot 10^{-3}\, m_0 c$. We deduce that in this sample 93(5) % of the positrons annihilate in defect-free MnSi and hence $\eta_{\text{b}}(x) = 0.93 \cdot f_x$ for the other samples. Consequently, the residual fraction $\eta_{\text{VMn}}(x) = 1 - \eta_{\text{b}}(x)$ depicted in Fig. 2(c) is attributed to positrons annihilating in V_{Mn}. We finally determined the concentration $c_{\text{VMn}}(x) = (\eta_{\text{b}}(x)^{-1} - 1)/(\tau_{\text{b}}\mu_{\text{VMn}})$, shown in Fig. 2(d), by adapting the commonly used trapping model [34]. Here, we used the calculated bulk lifetime $\tau_{\text{b}} = 111$ ps and an assumed trapping coefficient $\mu_{\text{VMn}} = 5 \cdot 10^{14}\,\text{s}^{-1}$ (Typical values of μ are between $10^{14}\,\text{s}^{-1}$ and $10^{15}\,\text{s}^{-1}$ [34]).

PALS spectra, exemplary shown in Fig. 2(b), display the same trend. For $x \leq 0$ only one lifetime component is found with $\tau_{\text{VMn}} = 185(4)$ ps in excellent agreement with the calculated value of 181 ps for a positron trapped in V_{Mn}. For $x = 0.04$, τ_{VMn} contributes only with an intensity of 8.5 % to the lifetime

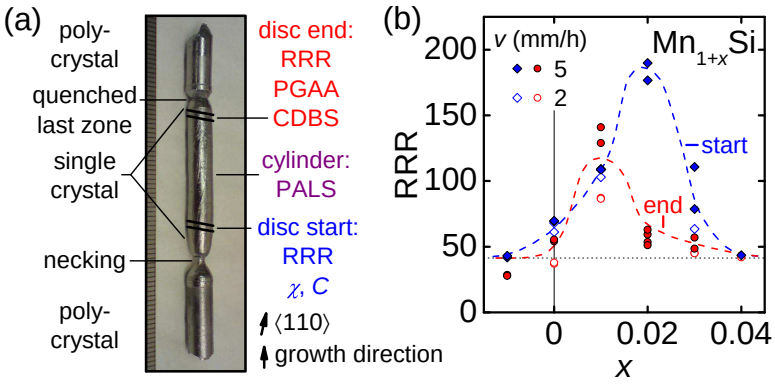

Figure 1: (Color online) Preparation of the MnSi specimens. (a) Photograph of a float-zoned ingot. Single-crystal discs from the start and the end as well as the remaining cylinders were studied. (b) RRR as function of the initial Mn excess x for different growth rates v. Samples from the same disc exhibit very similar RRRs. Dashed lines are guides to the eye. Here and in the following figures, data acquired on discs from start, end, and the cylinders are represented respectively.

spectrum and the dominant extracted lifetime $\tau_{\mathrm{b}} = 119(3)\,\mathrm{ps}$ is close to the calculated bulk value of 111 ps. Both lifetimes, τ_{VMn} and τ_{b}, were fixed for analyzing the remaining crystals. Here, we determined the intensity, $I_{\mathrm{VMn}}(x)$, shown in Fig. 2(c) arising from annihilation in $\mathrm{V_{Mn}}$ for the different samples using the fitted positron trapping rate $\kappa_{\mathrm{VMn}}(x)$ from bulk into $\mathrm{V_{Mn}}$. As in CDBS, for $x > 0$ annihilation in both defect-free bulk and $\mathrm{V_{Mn}}$ is observed, which allowed us to calculate the concentration $c_{\mathrm{VMn}}(x) = \kappa_{\mathrm{VMn}}(x)/\mu_{\mathrm{VMn}}$, shown in Fig. 2(d).

The values of c_{VMn} obtained in cylinders by PALS and discs by CDBS agree very well implying a homogeneous distribution of $\mathrm{V_{Mn}}$ along the cylindrical samples. For $x \leq 0$ only a lower limit of $2 \cdot 10^{-3}$ may be given for c_{VMn} due to saturation trapping of positrons in $\mathrm{V_{Mn}}$. For $x = 0.04$, the minimal vacancy

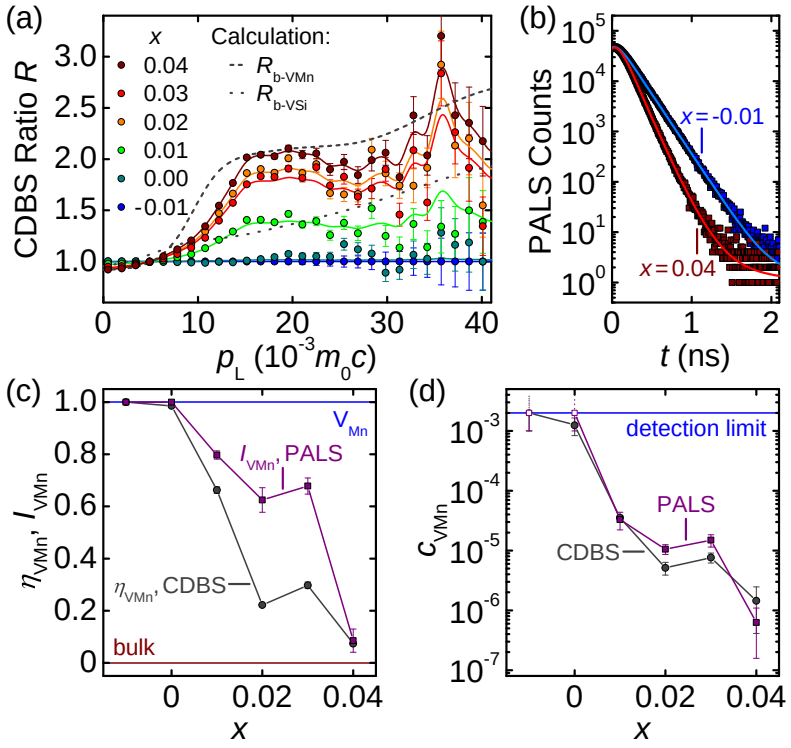

Figure 2: (Color online) Results of the positron annihilation spectroscopy. (a) CDBS ratio curves R_{x} as function of the longitudinal momentum component p_{L}. Solid lines represent linear superpositions of $R_{-0.01}$ and $R_{0.04}$, dashed lines the calculated curves $R_{\mathrm{b\text{-}VMn}}$ and $R_{\mathrm{b\text{-}VSi}}$. (b) PALS spectra together with fits to the data (solid lines). (c) Fraction η_{VMn} and PALS intensity I_{VMn} of positrons annihilating in Mn vacancies, $\mathrm{V_{Mn}}$, as function of x. (d) Concentration c_{VMn} of $\mathrm{V_{Mn}}$ obtained from CDBS and PALS.

(a) formation energy (eV)

type	Si-rich	stoich.	Mn-rich
V_{Mn}	0.50	1.29	1.94
V_{Si}	3.75	2.97	2.32
Si_{Mn}	0.00	1.57	2.87
Mn_{Si}	2.87	1.29	0.00

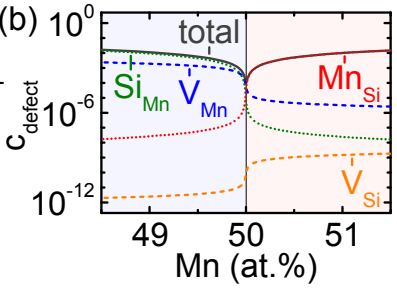

Figure 3: (Color online) Calculations of point defect energetics. (a) Effective formation energies in MnSi with different composition. (b) Expected defect concentrations as a function of composition for MnSi around its melting temperature.

concentration of $c_{\mathrm{VMn}} \approx 1 \cdot 10^{-6}$ establishes that an initial Mn excess efficiently suppresses the formation of $\mathrm{V_{Mn}}$ during crystal growth.

In the appropriate grand-canonical theory [35], the internal energies of the relaxed point defect configurations yield effective formation energies for the respective defect species. Their calculated values, as summarized in Fig. 3(a), show that MnSi belongs to the class of compounds with antisite accommodation of deviations from stoichiometry (with the defect energetics described by the two dimensionless parameters $\xi = 0.495$ and $\eta = -0.318$) [36]. Specifically, also on the Si-rich side deviations from stoichiometry are accommodated as antisites. Still, as in this situation the thermal formation of $\mathrm{V_{Mn}}$ is very inexpensive, a copious equilibrium concentration of $\mathrm{V_{Mn}}$ is expected at the elevated temperatures during growth as illustrated in Fig. 3(b). Diffusion measurements on MnSi have not been reported yet, but data on the isostructural FeSi suggest that diffusion in B20 compounds is extremely slow [37]. Hence, large thermal vacancy concentrations will be frozen in during cooling already at high temperatures.

The results of the positron annihilation experiments in combination with the calculated formation energies of point defects allow us to interpret the RRR shown in Fig. 1(b). For starting compositions of $x \leq 0.01$, Si antisites ($\mathrm{Si_{Mn}}$) and frozen-in thermal vacancies on the Mn sublattice ($\mathrm{V_{Mn}}$) are the dominant defect types leading to a low RRR. Around $x \approx 0.015$, at the maximum of the RRR, a pronounced drop of c_{VMn} is detected which indicates a transition from Mn-deficient to stoichiometric crystals with a minimal total concentration of defects. The shift with respect to $x = 0$ is attributed to the evaporation of Mn during growth. For $x \geq 0.02$, c_{VMn} further decreases as observed by CDBS and PALS. Inferred from the effective formation energies, the low RRR in this Mn-rich regime is mainly attributed to Mn antisites on the Si sublattice ($\mathrm{Mn_{Si}}$). It is noteworthy that contributions from vacancies on the Si sublattice ($\mathrm{V_{Si}}$) are neither detected experimentally nor expected from calculations. Contributions to the RRR arising from scattering on impurity atoms are assumed to be similar for all samples studied.

Figure 4 finally addresses the magnetic properties of different samples at temperatures around the helimagnetic phase transition. The specific heat as a function of temperature shown in Fig. 4(a) is qualitatively very similar for all samples. With decreasing temperature a broad maximum is associated with the fluctuation-disordered (FD) regime, while a sharp peak marks the first-order transition at T_c. These findings are corroborated by the magnetic ac susceptibility, see Fig. 4(b), where a point of inflection at T_2 defines the crossover from the paramagnet at high temperatures to the FD regime [38–40].

As shown in Fig. 4(c), with decreasing concentration of Mn vacancies, c_{VMn}, both T_c and T_2 monotonically decrease. The temperature range of the FD

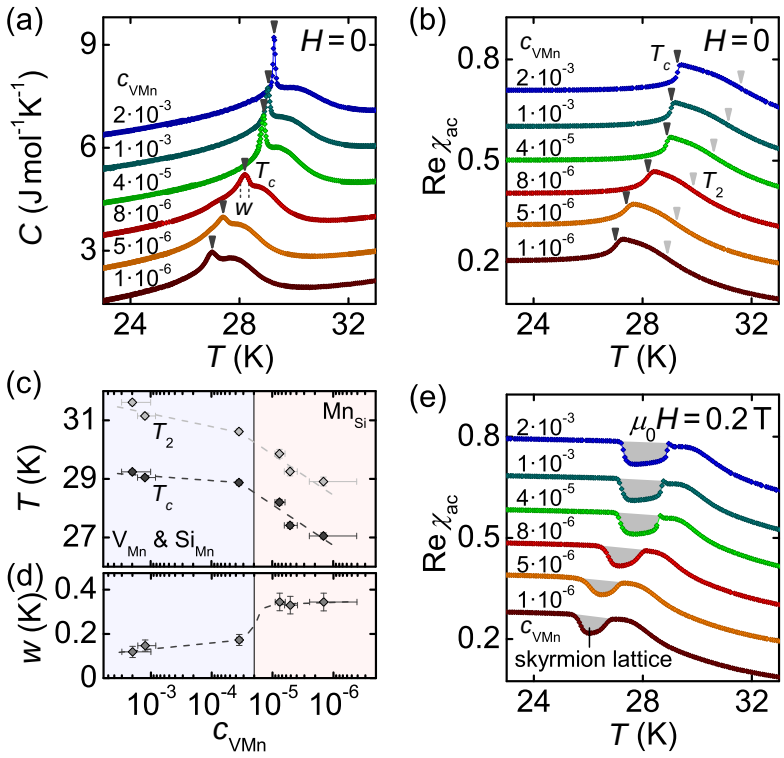

Figure 4: (Color online) Magnetic properties of MnSi with different defect concentrations as determined by positron spectroscopy. (a),(b) Temperature dependence of the specific heat, C, and the real part of the ac susceptibility, $\mathrm{Re}\,\chi_{\mathrm{ac}}$, for samples with different concentrations of Mn vacancies, c_{VMn}. (c) Transition temperatures T_c and T_2 as function of c_{VMn}. We distinguish two regimes with different dominant defect species. (d) Temperature width, w, of the transition at T_c as function of c_{VMn}. (e) Susceptibility in finite fields applied along $\langle 100 \rangle$ with a minimum attributed to a skyrmion lattice state (gray shading). Data have been offset for clarity.

regime, $T_2 - T_c$, remains essentially unchanged. In addition, the transition at T_c broadens as indicated by the full temperature width at half maximum, w, of the specific heat anomaly depicted in Fig. 4(d). A prominent change of slope around $c_{\mathrm{VMn}} = 2 \cdot 10^{-5}$ divides our samples in two groups with either high or low concentration of Mn vacancies. As established above, Si-rich samples are dominated by Mn vacancies and Si antisites (high c_{VMn}, blue shading) while Mn-rich specimens are dominated by Mn antisites (low c_{VMn}, red shading). Taken together, our findings imply that in particular Mn antisite disorder leads to a suppression of the transition temperatures accompanied by a smearing of the first-order transition at T_c. Still, as depicted in Fig. 4(e), all samples investigated show a plateau of reduced susceptibility just below T_c in an applied field of 0.2 T. This signature is characteristic of the skyrmion lattice state.

The shift of T_c and T_2 suggests that Mn antisites directly modify the electronic structure and in turn potentially all magnetic interactions. Apparently, ferromagnetic ordering is weakened by this kind of defects. Understanding the microscopic mechanisms, however, will require ab-initio calculations (see e.g. Ref. [41]). We finally note that in MnSi defect concentrations of 10^{-3} and 10^{-6} translate to mean defect distances of 5 and 50 lattice constants, respectively, as compared to the helix wavelength of 180 corresponding to 40 lattice constants. Bearing in mind the very large magnetic correlation length of $\sim 10^4$ in bulk MnSi, defect-related pinning of magnetic textures is expected mainly in form of (weak) collective pinning [42].

Conclusion

We have combined measurements of the magnetic bulk properties, RRR, positron annihilation spectroscopy, and calculations of effective defect formation energies in order to identify the species of point defects and their influence on magnetic and transport properties in a series of single crystals of MnSi. Using this approach we gained a detailed picture of characteristic lattice defects. Beside antisites on both sublattices, vacancies on the Mn sublattice are immanent in the system, where the dominant type of defects can be tuned by the initial Mn content. The magnetic properties of MnSi are qualitatively extremely robust to the defect concentration including the formation of the skyrmion lattice state. However, Mn antisites shift the transition temperatures to lower values and broaden the first-order transitions. Similar consequences may also be expected for the emergent phenomena of the skyrmion lattice. These new findings can serve as benchmark for microscopic theories on the complex magnetic behavior of MnSi. Hence, albeit the RRR may essentially reflect the absolute density of defects, the knowledge on the type of defects is key when characterizing single crystals of MnSi.

Methods

Measured Parameters

x	RRR		PAS Observables		c_{VMn}		Magnetic Transition		
	start	end	η_{VMn}	I_{VMn}	discs	cylinders	T_{c}(K)	T_2(K)	w(K)
-0.01	42.5	28.1	1.00	1.00	$> 2 \cdot 10^{-3}$	$> 2 \cdot 10^{-3}$	29.2	31.6	0.12
0.00	69.6	54.8	0.99	1.00	$1.2 \cdot 10^{-3}$	$> 2 \cdot 10^{-3}$	29.0	31.1	0.15
0.01	109	135	0.66	0.80	$3.5 \cdot 10^{-5}$	$3.3 \cdot 10^{-5}$	28.9	30.6	0.17
0.02	183	56.7	0.22	0.62	$5.1 \cdot 10^{-6}$	$1.0 \cdot 10^{-5}$	27.4	29.3	0.33
0.03	94.7	52.7	0.30	0.68	$7.6 \cdot 10^{-6}$	$1.5 \cdot 10^{-5}$	28.2	29.9	0.34
0.04	43.5	41.9	0.074	0.044	$1.4 \cdot 10^{-6}$	$6.3 \cdot 10^{-7}$	27.1	28.9	0.34

Table 1: Physical parameters of the investigated MnSi single crystals: Initial Mn excess x of sample preparation, RRR at start and end of crystals, PAS observables η_{VMn} and I_{VMn} determined from CDBS and PALS, respectively, (with values of 1.00 displaying saturation trapping of positrons in $\mathrm{V_{Mn}}$), vacancy concentrations c_{VMn} in discs and cylinders, transition temperatures T_c and T_2 as well as the temperature width w of T_c.

All measured quantities are summarized in Tab. 1. The principles of the applied experimental techniques and the accompanying theoretical calculations are explained in the following.

Crystal Preparation and Characterization

All crystal growth was carried out after evacuating the furnaces to about 10^{-7} mbar and filling them with 1.5 bar of 6N Ar treated with a point-of-use gas purifier [43]. First, high-purity elements (precast 4N Mn and 6N Si) were alloyed in an inductively heated furnace and cooled down in less than 5 min. In order to ensure compositional homogeneity, the resulting ingots were flipped and remolten three times before being cast to polycrystalline feed rods. Two rods of identical starting composition were optically float-zoned at a rate of 2 mm/h or 5 mm/h, respectively, while feed and seed rod were counter-rotating at 6 rpm. A necking during the first millimeters of growth promoted grain selection. Despite the argon atmosphere, the high vapor pressure of Mn leads to small losses. All growth attempts produced single crystals of 6 mm diameter and 10–30 mm length with no preferred direction of growth as determined by X-ray Laue diffraction. From the start and the end of the single crystals, see Fig. 1(a), we cut discs of 1 mm thickness perpendicular to $\langle 110 \rangle$ using a wire saw. From each disc we prepared two platelets of $\sim 5 \times 1 \times 0.2\,\mathrm{mm}^3$ with their long edge along $\langle 100 \rangle$.

The RRR of these samples was measured in a 4-terminal configuration using a bespoke dipstick in a liquid helium dewar and a standard lock-in technique. Specific heat, C, and magnetic ac susceptibility, $\mathrm{Re}\,\chi_{\mathrm{ac}}$, were measured in a QD-PPMS on cubes of 1 mm edge length prepared from the start discs. For the

specific heat we used a quasi-adiabatic heat pulse method where pulses had a size of 30% of the sample temperature [40]. The susceptibility was measured at an excitation frequency of 911 Hz with an amplitude of 1 mT.

Positron Annihilation Spectroscopy

In general, open-volume defects such as vacancies can trap positrons prior to annihilation leading to longer lifetimes than in the bulk due to the locally reduced electron density. PALS allows to detect the resulting annihilation rates and attribute them to defect-free bulk or vacancies [44]. In CDBS [45,46] measuring the energy of both annihilation γ-quanta yields the Doppler shift $\Delta E = \frac{1}{2} p_{\mathrm{L}} c$ caused by the longitudinal momentum component, p_{L}, of the annihilating pair. In vacancies ΔE is smaller than in bulk due to the lower overlap of the localized positron wave function with high-momentum core electrons. Furthermore, due to the intrinsically low background, CDBS allows to examine the chemical surrounding of vacancies [45].

CDBS was performed at the high-intensity positron beamline NEPOMUC at MLZ [47,48] with an incident positron energy of 25 keV corresponding to a mean implantation depth of 1.3 μm in MnSi. Beforehand, we confirmed that the bulk of the samples was probed by variation of the beam energy. Complementary PALS was carried out at the GIPS facility by generating positrons in the bulk of the cylindrical samples from a high-energy pulsed γ-beam [49]. The lifetime spectra were detected in a coincidence setup and analyzed by least-square fits.

In addition, we calculated CDB spectra and positron lifetimes in MnSi for annihilation in bulk as well as in vacancies $\mathrm{V_{Mn}}$ and $\mathrm{V_{Si}}$ on the Mn and Si sublattices. We used the MIKA Doppler program [50], which computes the positron wave function with a two-component density functional theory in the limit of a vanishing positron density [51] and describes the electron density based on an atomic superposition method [52]. After convolution of the calculated spectra with the experimental resolution, the bulk CDB ratio curves $R_{\mathrm{b\text{-}VMn}}$ and $R_{\mathrm{b\text{-}VSi}}$ were evaluated using spectra for $\mathrm{V_{Mn}}$ and $\mathrm{V_{Si}}$ as reference.

Ab-initio Calculations on Point Defects

Point defect energetics were calculated via density-functional theory (PBE-generalized gradient approximation [53]) as implemented in the ABINIT code using the projector-augmented wave framework [54]. We used a plane-wave cut-off of 30 Ha and a shifted fcc k-point grid corresponding to 32 points in the Brillouin zone of the ideal B20 simple cubic unit cell. For the defect-free system, the lattice constant yielded $a = 4.499$ Å, compared to the room temperature experimental value of 4.560 Å [55]. For the point defect calculations, a bcc arrangement with four eight-atom B20 cells per supercell was chosen, with one of these 32 atoms either removed or substituted by the other constituent element. Atomic positions were relaxed under fixed supercell dimensions. As the relevant temperature range for point defect creation and removal is far above the magnetic ordering temperature, no spin polarization was allowed.

References

[1] Mühlbauer, S. *et al.* Skyrmion Lattice in a Chiral Magnet. *Science* **323**, 915 (2009).

[2] Münzer, W. *et al.* Skyrmion lattice in the doped semiconductor $Fe_{1-x}Co_xSi$. *Phys. Rev. B* **81**, 041203 (R) (2010).

[3] Pfleiderer, C. *et al.* Skyrmion lattices in metallic and semiconducting B20 transitionmetal compounds. *J. Phys.: Condens. Matter* **22**, 164207 (2010).

[4] Yu, X. Z. *et al.* Real-space observation of a two-dimensional skyrmion crystal. *Nature (London)* **465**, 901 (2010).

[5] Yu, X. Z. *et al.* Near room-temperature formation of a skyrmion crystal in thin-filmsof the helimagnet FeGe. *Nature Mater.* **10**, 106 (2011).

[6] Seki, S., Yu, X. Z., Ishiwata, S. & Tokura, Y. Observation of Skyrmions in a Multiferroic Material. *Science* **336**, 198 (2012).

[7] Adams, T. *et al.* Long-Wavelength Helimagnetic Order and Skyrmion Lattice Phase in Cu_2OSeO_3. *Phys. Rev. Lett.* **108**, 237204 (2012).

[8] Nagaosa, N. & Tokura, Y. Topological properties and dynamics of magnetic skyrmions. *Nature Nano.* **8**, 899 (2013).

[9] Schwarze, T. *et al.* Universal helimagnon and skyrmion excitations in metallic, semiconductingand insulating chiral magnets. *Nature Mater.* **14**, 478 (2015).

[10] Tokunaga, Y. *et al.* A new class of chiral materials hosting magnetic skyrmions beyondroom temperature. *arXiv:1503.05651* (2015).

[11] Schulz, T. *et al.* Emergent electrodynamics of skyrmions in a chiral magnet. *Nature Phys.* **8**, 301 (2012).

[12] Jonietz, F. *et al.* Spin Transfer Torques in MnSi at Ultralow Current Densities. *Science* **330**, 1648 (2010).

[13] Yu, X. Z. *et al.* Skyrmion flow near room temperature in an ultralow current density. *Nat. Commun.* **3**, 988 (2012).

[14] Okamoto, H. Mn-Si (Manganese-Silicon). *J. Phase Equilib.* **12**, 505 (1991).

[15] Doiron-Leyraud, N. *et al.* Fermi-liquid breakdown in the paramagnetic phase of a pure metal. *Nature (London)* **425**, 595 (2003).

[16] Pfleiderer, C., Julian, S. R. & Lonzarich, G. G. Non-Fermi-liquid nature of the normal state of itinerant-electron ferromagnets. *Nature (London)* **414**, 427 (2001).

[17] Pfleiderer, C. On the Identification of Fermi-Liquid Behavior in Simple Transition Metal Compounds. *J. Low Temp. Phys.* **147**, 231 (2007).

[18] Pfleiderer, C. Experimental studies of weakly magnetic transition metal compounds. *J. Magn. Magn. Mater.* **226-230**, 23 (2001).

[19] Stishov, S. M. & Petrova, A. E. Itinerant helimagnet MnSi. *Phys.-Usp.* **54**, 1117 (2011).

[20] Bauer, A. & Pfleiderer, C. Magnetic phase diagram of MnSi inferred from magnetization and acsusceptibility. *Phys. Rev. B* **85**, 214418 (2012).

[21] Ritz, R. *et al.* Giant generic topological Hall resistivity of MnSi under pressure. *Phys. Rev. B* **87**, 134424 (2013).

[22] Iwasaki, J., Mochizuki, M. & Nagaosa, N. Universal current-velocity relation of skyrmion motion in chiral magnets. *Nat. Commun.* **4**, 1463 (2013).

[23] Lin, S.-Z., Reichhardt, C., Batista, C. D. & Saxena, A. Particle model for skyrmions in metallic chiral magnets: Dynamics, pinning, and creep. *Phys. Rev. B* **87**, 214419 (2013).

[24] Müller, J. & Rosch, A. Capturing of a magnetic skyrmion with a hole. *Phys. Rev. B* **91**, 054410 (2015).

[25] Milde, P. *et al.* Unwinding of a Skyrmion Lattice by Magnetic Monopoles. *Science* **340**, 1076 (2013).

[26] Ritz, R. *et al.* Formation of a topological non-Fermi liquid in MnSi. *Nature (London)* **497**, 231 (2013).

[27] Neubauer, A. *et al.* Ultra-high vacuum compatible image furnace. *Rev. Sci. Instrum.* **82**, 013902 (2011).

[28] Bauer, A. *Investigation of itinerant antiferromagnets and cubic chiral helimagnets.* Ph.D. thesis, Technische Universität München (2014).

[29] Révay, Z., Kudějová, P., Kleszcz, K., Söllradl, S. & Genreith, C. In-beam activation analysis facility at MLZ, Garching. *Nucl. Instrum. Meth. A* **799**, 114 (2015).

[30] Tang, Z., Hasegawa, M., Nagai, Y. & Saito, M. Density functional study on metastable bcc copper: Electronic structureand momentum density of positron-electron pairs. *Phys. Rev. B* **65**, 195108 (2002).

[31] Makkonen, I., Hakala, M. & Puska, M. J. First-principles calculation of positron states and annihilation at defects in semiconductors. *Physica B* **376–377**, 971 (2006).

[32] Makkonen, I., Hakala, M. & Puska, M. J. Modeling the momentum distributions of annihilating electron-positronpairs in solids. *Phys. Rev. B* **73**, 035103 (2006).

[33] Reiner, M., Gigl, T. & Hugenschmidt, C. Ab-initio calculation of CDB spectra - a case study on transitionmetals. *J. Phys.: Conf. Ser.* **505**, 012025 (2014).

[34] Hautojärvi, P. & Corbel, C. Positron Spectroscopy of Defects in Metals and Semiconductors. In Dupasquier, A. & Mills jr., A. P. (eds.) *Positron Spectroscopy of Solids*, vol. 125 of *Proceedings of the International School of Physics "Enrico Fermi"*, 491 (IOS Press, Amsterdam, 1995).

[35] Meyer, B. & Fähnle, M. Atomic defects in the ordered compound $B2$-NiAl: A combination of ab initio electron theory and statistical mechanics. *Phys. Rev. B* **59**, 6072 (1999).

[36] Leitner, M. Thermodynamics of point defects and diffusion mechanisms in B2-ordered compounds. *arXiv:1503.03798* (2015).

[37] Salamon, M. & Mehrer, H. Diffusion in the B20-type phase FeSi. *Philos. Mag. A* **79**, 2137 (1999).

[38] Bauer, A. *et al.* Quantum phase transitions in single-crystal $Mn_{1-x}Fe_xSi$ and $Mn_{1-x}Co_xSi$: Crystal growth, magnetization, ac susceptibility, and specific heat. *Phys. Rev. B* **82**, 064404 (2010).

[39] Janoschek, M. *et al.* Fluctuation-induced first-order phase transition in Dzyaloshinskii-Moriya helimagnets. *Phys. Rev. B* **87**, 134407 (2013).

[40] Bauer, A., Garst, M. & Pfleiderer, C. Specific Heat of the Skyrmion Lattice Phase and Field-Induced Tricritical Point in MnSi. *Phys. Rev. Lett.* **110**, 177207 (2013).

[41] Franz, C. *et al.* Real-Space and Reciprocal-Space Berry Phases in the Hall Effect of $Mn_{1-x}Fe_xSi$. *Phys. Rev. Lett.* **112**, 186601 (2014).

[42] Adams, T. *et al.* Long-Range Crystalline Nature of the Skyrmion Lattice in MnSi. *Phys. Rev. Lett.* **107**, 217206 (2011).

[43] SAES Pure Gas, MicroTorr MC190-902F. http://www.saespuregas.com.

[44] Coleman, P. *Positron beams and their applications* (World Scientific, 2000).

[45] Asoka-Kumar, P. *et al.* Increased Elemental Specificity of Positron Annihilation Spectra. *Phys. Rev. Lett.* **77**, 2097 (1996).

[46] Mijnarends, P. E., Kruseman, A. C., van Veen, A., Schut, H. & Bansil, A. Two-detector Doppler broadening study of enhancement in Al. *J. Phys.: Condens. Mat.* **10**, 10383 (1998).

[47] Hugenschmidt, C., Piochacz, C., Reiner, M. & Schreckenbach, K. The NEPOMUC upgrade and advanced positron beam experiments. *New J. Phys.* **14**, 055027 (2012).

[48] Reiner, M., Pikart, P. & Hugenschmidt, C. In-situ (C)DBS at high temperatures at the NEPOMUC positron beam line. *J. Phys.: Conf. Ser.* **443**, 012071 (2013).

[49] Butterling, M. *et al.* Gamma-induced Positron Spectroscopy (GiPS) at a superconducting electron linear accelerator. *Nucl. Instrum. Meth. B* **269**, 2623 (2011).

[50] Torsti, T. *et al.* Three real-space discretization techniques in electronic structure calculations. *Phys. Status Solidi B* **243**, 1016 (2006).

[51] Puska, M. J. & Nieminen, R. M. Theory of positrons in solids and on solid surfaces. *Rev. Mod. Phys.* **66**, 841 (1994).

[52] Puska, M. J. & Nieminen, R. M. Defect spectroscopy with positrons: a general calculational method. *J. Phys. F: Met. Phys.* **13**, 333 (1983).

[53] Perdew, J. P., Burke, K. & Ernzerhof, M. Generalized Gradient Approximation Made Simple. *Phys. Rev. Lett.* **77**, 3865 (1996).

[54] Gonze, X. *et al.* ABINIT: First-principles approach to material and nanosystem properties. *Comput. Phys. Commun.* **180**, 2582 (2009).

[55] Stishov, S. M. *et al.* Heat capacity and thermal expansion of the itinerant helimagnet mnsi. *Journal of Physics: Condensed Matter* **20**, 235222 (2008).

Acknowledgements

We thank K. Lochner, S. Mayr, C. Schnarr, and S. Zeytinoglu for assistance with the experiments and P. Böni for fruitful discussions. Financial support through BMBF project no.05K13WO1, DFG TRR80, DFG FOR960, and ERC AdG (291079, TOPFIT) is gratefully acknowledged.

Author contributions statement

M.R., A.B., and C.H. initiated the PAS experiments on defects in MnSi. M.R., A.B., and M.L. wrote the paper. A.B. grew all crystals and characterized their transport and magnetic properties. M.R. and T.G. carried out the (C)DBS experiments. M.R., W.A., M.B. and A.W. performed the PALS experiments. M.R. analyzed all data from (C)DBS and PALS experiments. P.K. was responsible for the PGAA measurements. Ab-initio calculations of the defect thermodynamics have been performed by M.L. C.P. and C.H. substantially contributed to the discussion and to the writing of the manuscript. All the authors have read the manuscript and agree with its content.

Additional information

Competing financial interests The authors declare that they have no competing financial interests.